Demonstration of an On-Chip TE-Pass Polarizer Based on Radiation Coupling

Li Zhang, Shengjie Tang, Cheng Chen, Haibin Lv, and Xiaoping Liu

Abstract—**An on-chip, high-extinction-ratio transverse electric (TE) pass polarizer utilizing a silicon oxynitride (SiON) slab has been proposed and experimentally verified. The power confinement ratio of the mode field is manipulated by using a SiON slab, where most of the power of the transverse magnetic (TM) mode is transferred to the upper SiON slab and then attenuated through radiation, while the TE mode passes through with relatively low propagation loss. Experimental results show that our proposed device can achieve an extinction ratio that varies from 20.5 to 32.7 dB in the wavelength range of 790 to 870 nm, with an insertion loss of 0.6 to 1.7 dB. Potentially, this design has lower material refractive index contrast, larger minimum etching size, smaller lengths, and less stray light crosstalk, which is beneficial for systems applications such as gyroscopes.**

Index Terms—**On-chip polarizer, radiation coupling, less stray light crosstalk.**

I. Introduction

In recent years, integrated photonics has emerged as a key player in the development of low-power and high-bandwidth interconnection systems, owing to its compatibility with complementary metal oxide semiconductor (CMOS) processes [1]. However, for certain photon sensors, various polarization disturbances significantly impact their performance [2], necessitating precise control of transverse electric (TE) and transverse magnetic (TM) modes for optimal functionality. To address this problem, various solutions have been proposed, including the usage of polarization-independent devices [3], [4], [5], polarization-beam splitters [6], [7], [8], [9], [10], [11], [12], and polarization-rotating devices [13], [14], [15], [16]. Another critical approach involves the usage of on-chip polarizers, which eliminate unwanted polarization states, enabling the on-chip system to operate in a single state of polarization.

Over the years, various polarizers have been reported, as shown in Table I. In principle, they include polarizers using subwavelength grating structures [17], [18], [19], [20], [21], [22], [23], hybrid plasma [24], [25], [26], [27], directional couplers [28], [29], [30], anisotropic equivalent medium [31], [32], and bending radiation [33], [34], [35], [36]. However, most of these devices require the use of complex structures. For example, an ultra-broadband polarizer with an extinction ratio (ER) greater than 20 dB and an insertion loss (IL) less than 1 dB, designed and manufactured by Hongnan Xu et al. [31], uses a sub-wavelength grating structure that has a very small minimum etching size, which is not conducive to large-scale production and manufacturing. In addition, the principle of most polarizers is highly dependent on the birefringence of the waveguide itself, making it difficult to achieve the same high ER on lower refractive index platforms such as silicon nitride (SiN). To solve the problem of polarization at lower refractive index contrast waveguide, Bauters et al. [37] fabricates a TE-pass polarizer using ultra-thin SiN curved waveguides, achieving a high ER of 75 dB within the wavelength range of 1.5 to 1.62 μm. However, the ultralong structure of the waveguide is not conducive for system integration. Therefore, there is a pressing need for a new on-chip polarizer design with a larger minimum etching size, smaller lengths, and lower dependence on the birefringence of the waveguide itself, to provide a more convenient polarization scheme for lower refractive index contrast platforms.

To address these issues, we experimentally demonstrate a TE-pass polarizer by using a silicon oxynitride (SiON) slab fabricated on a SiN platform. The power of the TM mode in the SiN waveguide (SW) transfers to the upper SiON slab, while the TE mode passes through with relatively low loss. Our measured results indicate that within the wavelength range of 790 to 870 nm, the ER varies from 20.5 to 32.7 dB, and the IL ranges from 0.6 to 1.7 dB. Compared to other polarizer designs, our design presents a robust polarization solution for platforms with low refractive index contrast, requiring a larger minimal etching size of only 550 nm, and exhibiting relatively shorter lengths. Moreover, this polarization scheme enables the entry of scattered light into the SiON slab, effectively reducing crosstalk within the core layer. This is beneficial for systems applications such as gyroscopes.

II. Structure and Principle

The proposed TE-pass polarizer device, as shown in Fig. 1(a), is fabricated on a SiN platform with an up-cladding of silicon dioxide (SiO_2). The polarizing part of the device includes a SW, a SiO_2 intermediate layer with a thickness of g, and a slab made of SiON material. The slab has a width of W_s, a length of L, and a thickness of H_s, which is positioned at a distance, g, above the

Manuscript received 4 January 2024; revised 19 February 2024; accepted 9 March 2024. Date of publication 19 March 2024; date of current version 29 March 2024. This work was supported in part by the Science and Technology Commission of Shanghai Municipality under Grant 21DZ1101500 and in part by Start-up, ShanghaiTech University. *(Corresponding authors: Haibin Lv; Xiaoping Liu.)*

The authors are with the School of Physical Science and Technology, ShanghaiTech University, Shanghai 201210, China (e-mail: zhangli1@shanghaitech.edu.cn; tangshj@shanghaitech.edu.cn; chencheng@shanghaitech.edu.cn; lvhaibin203@163.com; liuxp1@shanghaitech.edu.cn).

Digital Object Identifier 10.1109/JPHOT.2024.3377707

TABLE I
SUMMARY OF PUBLISHED POLARIZERS

Core material	Polarization state	Refractive index contrast	Minimum etching size (nm)	Length (mm)	IL (dB)	$BW_{ER>20dB}$ (nm)
Si [17]	TE	High	150	0.009	< 0.5	60 (1520-1580)
Si [26]	TE	High	450	0.006	< 4.6	60 (1520-1580)
Si [31]	TE	High	60	0.013	< 1	415 (1260-1675)
SiN [37]	TE	Low	3500	54.14	< 0.3	120 (1500-1620)
Si [38]	TM	High	120	0.7	< 1	90 (1530-1620)
Si [39]	TM	High	115	0.017	< 0.9	415 (1260-1675)
Si [40]	TM	High	100	0.016	< 1.7	200 (1450-1650)
SiN [This work]	TE	Low	550	4.74	< 1.7	80 (790-870)

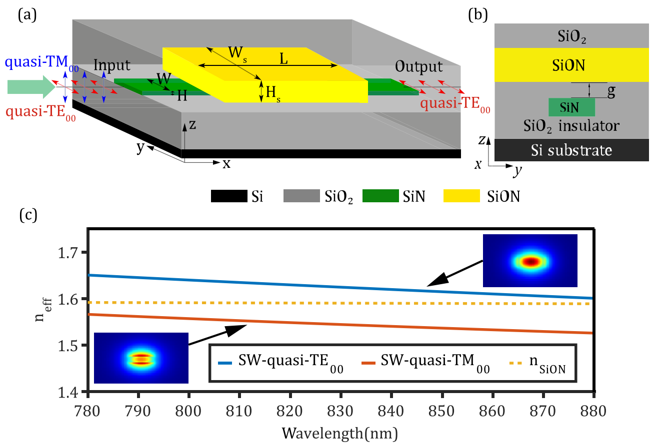

Fig. 1. (a) 3D schematic of the proposed TE-pass polarizer on a SiN platform. (b) Cross section of polarizer covered by SiON slab. (c) The n_{eff} for SW-quasi-TE_{00} mode and SW-quasi-TM_{00} mode as a function of the wavelength when W = 550 nm and H = 180 nm. Here, the dashed line represents the material refractive index of the SiON slab. The electric field profiles at $\lambda_0 = 830$ nm of the two modes are shown in the inset, respectively.

SW, as illustrated in the cross-sectional view of the slab area in Fig. 1(b).

To achieve a TE-pass polarizer, a SiON slab is introduced to extend the majority of the power of the quasi-TM_{00} mode into the SiON slab without affecting the power of the quasi-TE_{00}. The different power response to different polarizations depends on the refractive index of the SiON slab (n_{SiON}), which should satisfy the following inequality:

$$n_{eff}^{TM_{00}} < n_{SiON} < n_{eff}^{TE_{00}} \quad (1)$$

where $n_{eff}^{TE_{00}}(n_{eff}^{TM_{00}})$ is the effective refractive index (n_{eff}) of the quasi-TE_{00}(TM_{00}) mode in the SW without SiON slab. When $n_{SiON} < n_{eff}^{TE_{00}}$, the quasi-$TE_{00}$ mode power remains confined in the SW. Conversely, when $n_{eff}^{TM_{00}} < n_{SiON}$, the quasi-$TM_{00}$ mode power extends into the SiON slab. It's important to note that meeting these conditions simultaneously within the target wavelength range of 780–880 nm is necessary to obtain sufficient bandwidth. Additionally, the concept of power ratio (PR) is introduced to assess the extent of mode diffusion, representing the ratio of mode power within the SiN core region to the total mode power. A higher PR indicates superior confinement within the SiN core, while a lower PR suggests increased power diffusion.

The Finite Difference Eigenmode (FDE) and 3D bidirectional Eigenmode Expansion (EME) methods simulation methods using Lumerical commercial software are employed to design the polarizer and investigate its characteristics. FDE is utilized for computing mode energy distribution and bending losses per unit distance. The boundary condition employed is a Perfectly Matched Layer (PML), with the minimum grid accuracy dy = dz = 10 nm (where dx represents the direction of light propagation). In simulations for optical field transmission, we utilize EME. Here, PML is utilized for all boundary conditions except for the default metallic boundary conditions at the input and output terminals. The minimum grid accuracy is consistently maintained at dx = dy = dz = 10 nm. For the wavelengths centered around $\lambda_0 = 830$ nm, the material refractive indices of SiN and SiO_2 are around 2.022 and 1.453, respectively. With the material dispersion of SiN and SiO_2 taken into account, the n_{eff} for the SW-quasi-TE_{00}(TM_{00}) modes is calculated first and shown in Fig. 1(c). The width and thickness of the SiN core are $W = 550$ nm and $H = 180$ nm, ensuring that the n_{eff} of SW modes satisfies the inequality (1) across the entire wavelength range. Simultaneously, the electric field profiles for both modes are provided in the inset. Based on the aforementioned polarizer requirement of the inequality (1), n_{SiON} can be chosen and represented, for example, by the dashed line in Fig. 1(c), with a value of $n_{SiON} = 1.59$ at $\lambda_0 = 830$ nm. Of course, our design can operate in communication wavelength bands such as 1.3 μm and 1.55 μm, but adjustments of the key parameters such as n_{SiON}, W, and H are necessary to satisfy inequality (1). Moreover, an increase in SiON thickness H_s would theoretically lead to improved performance of the polarizer under the same parameters. However, concerning the fabrication constraints, we opted for $H_s = 1$ μm.

The thickness g of the SiO_2 intermediate layer determines the coupling strength between the SW and SiON slab, it significantly affects the PR of the modes, especially for the quasi-TM_{00} mode. Considering the SW and the upper SiON slab (the region indicated by the white box in Fig. 2(a) and (b)) as a hybrid waveguide (HW), the electric field profiles of the quasi-TE_{00} (TM_{00}) modes (calculated by FDE) in the HW has been shown in Fig. 2. It can be seen that the HW-quasi-TE_{00} mode (Fig. 2(a)) is mostly confined to the SW region, while the HW-quasi-TM_{00} (Fig. 2(b)) mode mostly extends to the SiON slab. Due to the weak coupling between SW-quasi-TE_{00} mode and SiON slab mode, SW-quasi-TE_{00} mainly excites the HW-quasi-TE_{00} mode, resulting in minimal power transfer to the slab. Conversely, due to the significant coupling between SW-quasi-TM_{00}

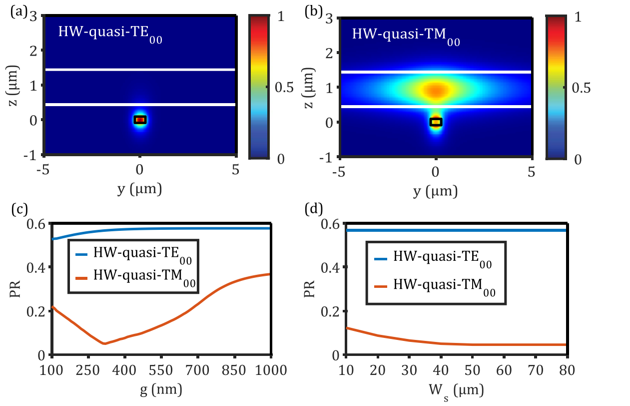

Fig. 2. Electric field profiles of (a) HW-quasi-TE_{00} and (b) HW-quasi-TM_{00} mode. Here, $n_{SiON} = 1.59$, $\lambda_0 = 830$ nm, and $g = 320$ nm. Variation of HW-quasi-TE_{00} (TM_{00}) mode PR for the (c) parameter g and (d) parameter Ws. Here, $W = 550$ nm, $n_{SiON} = 1.59$, and $\lambda_0 = 830$ nm.

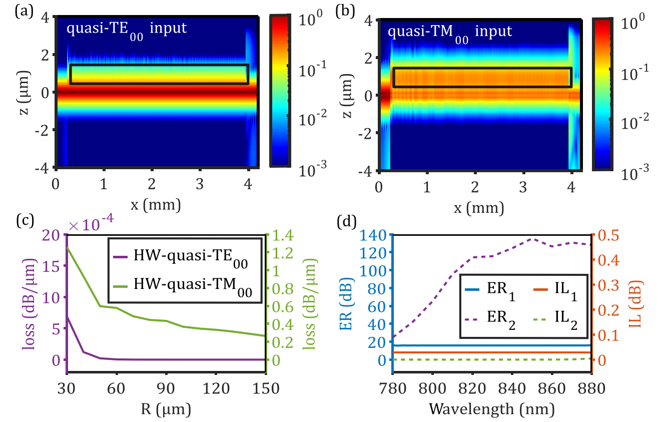

Fig. 3. Lateral view of light propagation at 830 nm wavelength through the polarizer for (a) quasi-TE $_{00}$ and (b) quasi-TM_{00} input. Here, $W = 550$ nm, $n_{SiON} = 1.59$, $Ws = 50$ μm, $g = 320$ nm, and $L = 3.69$ mm. (c) The variation of transmission loss per unit length with bending radius R. Here, $\lambda_0 = 830$ nm. (d) ER and IL as a function of wavelength. ER $_1$ and IL_1 are the results without bending and with a straight waveguide length of L = 3.69 mm. ER_2 and IL_2 are the results of the corresponding two 90° circular arc structures when the bending radius $R = 100$ μm.

mode and SiON slab mode, the SW-quasi-TM_{00} excites the HW-quasi-TM_{00} mode shown in Fig. 2(b). Therefore, the power of quasi-TM_{00} mode transferred to the slab is large and can reach the maximum by adjusting the parameter g. It should be noted that except for these two bounded fundamental modes, all other modes supported in the HW are leakage modes.

To find the optimal value of g, the PR as a function of g for both the HW-quasi-TE_{00} and HW-quasi-TM_{00} modes is shown in Fig. 2(c). As g increases, the PR of the HW-quasi-TE_{00} mode ($r_{TE_{00}}$) approaches saturation. Differently, the PR of the HW-quasi-TM_{00} mode ($r_{TM_{00}}$) first decreases and then increases with g increasing, with the minimum occurring around $g =$ 320 nm. Near this point, $r_{TE_{00}}$ exceeds 55% while $r_{TM_{00}}$ is less than 10%, indicating that the HW-quasi-TE_{00} mode is well confined in the SW region and the HW-quasi-TM_{00} mode is mainly distributed in the SiON slab. It should be noted that $r_{TM_{00}}$ can be reduced further with the increasing width of the SiON slab while $r_{TE_{00}}$ is almost unaffected, as is shown in Fig. 2(d). Moreover, Fig. 2(d) also suggests that both two ratios tend to be constant when W_s is large enough.

Further simulation has been conducted to verify the principle of this polarizer (see Fig. 3). It can be observed that the quasi-TE_{00} mode is almost losslessly transferred through the region covered by the SiON slab (indicated by the white box in Fig. 3(a)). Differently, the quasi-TM_{00} mode is attenuated significantly at the output end. Specifically, the coupling efficiency between the SW-quasi-TM_{00} mode and the HW-quasi-TM_{00} mode is approximately 15.8% (calculated by EME). The coupling occurs twice during the process of transmitting into and out of the SiON slab-covered region, resulting in a total power loss of about 16 dB, corresponding to the value at the wavelength of 830 nm on the solid line ER_1 in Fig. 3(d). Finally, the ER and IL without considering bending are calculated as a function of wavelength and shown as ER_1 and IL_1 (the solid lines) in Fig. 3(d) which are defined respectively as follows:

$$ER = 10 \times \log_{10}\left(\frac{P_{TE}}{P_{TM}}\right)$$
$$IL = -10 \times \log_{10}(P_{TE}) \qquad (2)$$

where P_{TE} and P_{TM} are the normalized output power for the SW-quasi-TE_{00} and SW-quasi-TM_{00} mode, respectively.

To further improve the ER, we introduced a curved structure. Fig. 3(c) shows the transmission losses per unit length of two HW modes as a function of the bending radius. Taking $R = 100$ μm as an example, the loss rate of the HW-quasi-TM $_{00}$ mode is 0.37 dB/μm while the loss rate of the HW-quasi-TE $_{00}$ mode is 3.3e-9 dB/μm. The corresponding ER and IL generated by the two modes after propagating through two 90° circular arc structures are 115 dB and 1e-6 dB, respectively. In addition, the spectra of the ER and IL after propagating through two 90° circular arc structures with $R = 100$ μm are shown as ER_2 and IL_2 (the dashed lines) in Fig. 3(d).

In practical manufacturing, deviations in width and thickness are two main factors affecting polarizer performance. To further elucidate the capabilities of our polarizer, tolerance analysis is presented in Fig. 4. It can be seen that when $\Delta W = \pm 10$ nm, $ER_1 + ER_2 > 25$ dB, and $IL_1 + IL_2 < 0.2$ dB are present throughout the entire wavelength range of 780-880 nm. Similarly, when $\Delta H = \pm 10$ nm, within the wavelength range of 815-880 nm, there are $ER_1 + ER_2 > 25$ dB and $IL_1 + IL_2 < 0.2$ dB. The aforementioned tolerance analysis demonstrates the good fabrication robustness of our polarizer.

III. Fabrication and Characterization

The designed TE-pass polarizer was fabricated on a SiN-on-insulator wafer consisting of a 180 nm thick top LPCVD SiN layer and a 2 μm thick buried-oxide layer. The waveguide structure was etched on the 180 nm thick SiN layer, followed by a 320 nm thick SiO $_2$ intermediate layer. Then, a 1 μm thick SiON film was deposited and unnecessary parts were etched. Finally, a 2 μm thick SiO $_2$ cladding was applied to the entire structure. As shown in Fig. 5, the SW has a total length of 4.74 mm (including four 90° circular arc structures with a radius of $R = 100$ μm), with about 3.69 mm straight waveguide and two 90° circular arc

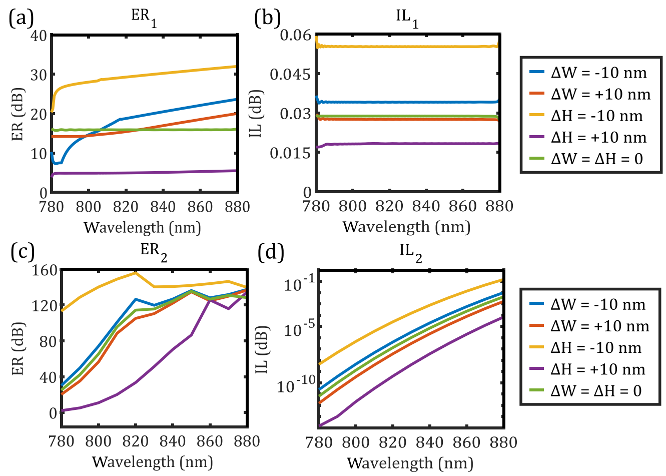

Fig. 4. Fabrication tolerance analysis. Calculated (a) ER_1, (b) IL_1, (c) ER_2, and (d) IL_2 spectra for the SiN waveguide width deviation $\Delta W = \pm 10$ nm and thickness deviation $\Delta H = \pm 10$ nm.

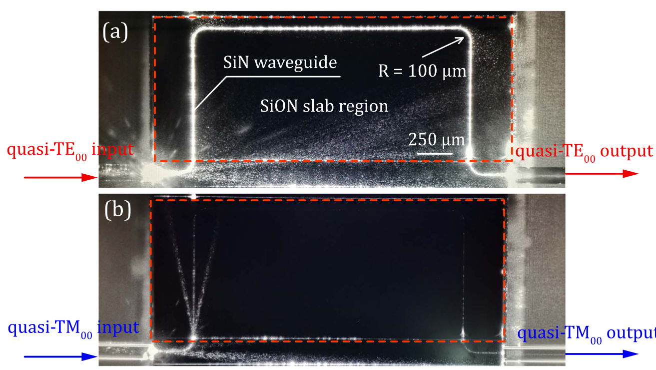

Fig. 5. Optical microscopy image of the fabricated polarizer with light injection. (a) quasi-TE_{00} input. (b) quasi-TM_{00} input.

structures ($R = 100$ μm) located below the SiON slab which is indicated by the red dashed box.

To evaluate the performance of the fabricated polarizer, a super luminescent diode (Thorlabs SLD-43664) with a central wavelength of 832.5 nm and an optical bandwidth of 62.1 nm was employed as the light source. An optic fiber polarization beam splitter (fiber-PBS) is used to generate a polarized light source with an ER of around 35 dB. Then, a polarization controller was utilized to switch between the TE and TM polarized incident light, which was coupled to the chip through the inverted taper structure at the input end of the polarizer. The output light was detected using an optical spectrum analyzer.

The ER and IL measurements of the polarizer are presented in Fig. 6. The influences of input and output edge couplers have been removed by subtracting the transmission spectra of reference waveguides. The measured ER was found to vary between 20.5 to 32.7 dB over the wavelength range of 790–870 nm, with an IL $<$ 1.7 dB for the range of 790-870 nm. Moreover, within the wavelength range of 806-870 nm, the ER is greater than 27.1 dB and the IL is less than 1.7 dB. The experimentally determined ER is significantly lower than the simulated ones, which could be ascribed to two factors. Firstly, due to the lack of enough lateral offset between the coupling input and output

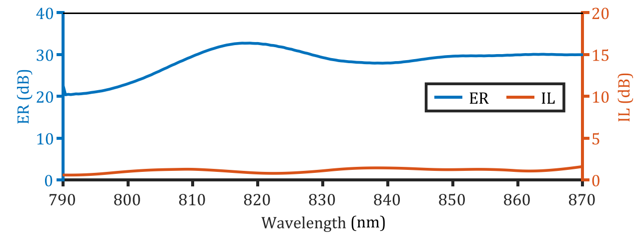

Fig. 6. Measured ER and IL of the polarizer.

ports, a portion of the scattered light from the input end and from the first waveguide bending was recoupled back into the output waveguide, causing additional polarization crosstalk and ultimately reducing ER during the measurement. Secondly, the utilized fiber-PBS in the measurement only generates polarized light with an ER of about 35 dB, leading to the limitation of detecting an ER higher than this value. In addition, the measured IL is overall about 1 dB larger than the theoretical IL. This is because the deviations of the thickness g of the SiO_2 intermediate layer and the refractive index of SiON from the design values will also increase the IL. To achieve smaller IL, it is possible to scan the thickness g of the intermediate layer and the refractive index of SiON, as well as use more advanced lithography and etching processes.

IV. Conclusion

In summary, we have proposed and experimentally demonstrated an on-chip TE-pass polarizer by using a SiON slab. By adjusting the parameter g and the refractive index of the SiON material, the quasi-TM_{00} mode field power is extended to the SiON slab, while the quasi-TE_{00} mode field power is well constrained in the SW. As a result, the quasi-TM_{00} mode is mainly attenuated through radiation, while the quasi-TE_{00} mode passes through with minimal loss. Within the wavelength range of 790 to 870 nm, the measured ER of the polarizer ranges from 20.5 to 32.7 dB, and the corresponding IL ranges from 0.6 to 1.7 dB. Additionally, this design reduces the dependence on the birefringence of the waveguide itself in principle, requiring a larger minimal etching size of only 550 nm, and exhibiting relatively shorter lengths compared to similar types, providing an alternative polarization scheme for platforms with lower refractive index contrast. It's important to note that despite achieving a reduction in length exceedingly tenfold compared to solutions on the same platform [37], there remains a necessity for further reducing the device length, especially considering the demand for large-scale integration. This reduction should be achieved without reducing ER or increasing IL. One effective approach is to increase the number of bends to replace long straight waveguides. This strategy leverages the fact that the bending transmission loss of HW-quasi-TM_{00} is significantly greater than that of HW-quasi-TE_{00}, thereby enabling further miniaturization while maintaining performance. Furthermore, this polarization scheme enables the entry of scattered light into the SiON slab, effectively reducing crosstalk within the core layer. This is beneficial for systems applications such as gyroscopes.

REFERENCES

[1] D. Thomson et al., "Roadmap on silicon photonics," *J. Opt.*, vol. 18, no. 7, Jun. 2016, Art. no. 073003.

[2] E. C. Kintner, "Polarization control in optical-fiber gyroscopes," *Opt. Lett.*, vol. 6, no. 3, pp. 154–156, Mar. 1981.

[3] Q. Deng, Q. Yan, L. Liu, X. Li, J. Michel, and Z. Zhou, "Robust polarization-insensitive strip-slot waveguide mode converter based on symmetric multimode interference," *Opt. Exp.*, vol. 24, no. 7, pp. 7347–7355, Apr. 2016.

[4] L. Liu, Q. Deng, and Z. Zhou, "Subwavelength-grating-assisted broadband polarization-independent directional coupler," *Opt. Lett.*, vol. 41, no. 7, pp. 1648–1651, Apr. 2016.

[5] Y. Chen and J. Xiao, "Ultracompact and broadband silicon-based polarization-independent 1 x 2 power splitter using a shallowly etched multimode interference coupler," *J. Opt. Soc. Amer. B.*, vol. 38, no. 10, pp. 3064–3070, Oct. 2021.

[6] J. Hou, L. Wang, C. Yang, B. Wang, and S. Chen, "Compact high extinction ratio asymmetric polarization beam splitter of periodic rods waveguide," *Appl. Opt.*, vol. 54, no. 34, pp. 10277–10282, Dec. 2015.

[7] C. Li and D. Dai, "Compact polarization beam splitter based on a three-waveguide asymmetric coupler with a 340-nm-Thick silicon core layer," *J. Lightw. Technol.*, vol. 36, no. 11, pp. 2129–2134, Jun. 2018.

[8] C. Li, M. Zhang, J. E. Bowers, and D. Dai, "Ultra-broadband polarization beam splitter with silicon subwavelength-grating waveguides," *Opt. Lett.*, vol. 45, no. 8, pp. 2259–2262, Apr. 2020.

[9] S. Chen, H. Wu, and D. Dai, "High extinction–ratio compact polarisation beam splitter on silicon," *Electron. Lett.*, vol. 52, no. 12, pp. 1043–1045, Jun. 2016.

[10] Y. Kim, M. H. Lee, Y. Kim, and K. H. Kim, "High-extinction-ratio directional-coupler-type polarization beam splitter with a bridged silicon wire waveguide," *Opt. Lett.*, vol. 43, no. 14, pp. 3241–3244, Jul. 2018.

[11] H. Wu, Y. Tan, and D. Dai, "Ultra-broadband high-performance polarizing beam splitter on silicon," *Opt. Exp.*, vol. 25, no. 6, pp. 6069–6075, Mar. 2017.

[12] H. Zafar, R. Flores, R. Janeiro, A. Khilo, M. S. Dahlem, and J. Viegas, "High-extinction ratio polarization splitter based on an asymmetric directional coupler and on-chip polarizers on a silicon photonics platform," *Opt. Exp.*, vol. 28, no. 15, pp. 22899–22907, Jul. 2020.

[13] L. Gao, Y. Huo, J. S. Harris, and Z. Zhou, "Ultra-compact and low-loss polarization rotator based on asymmetric hybrid plasmonic waveguide," *IEEE Photon. Technol. Lett.*, vol. 25, no. 21, pp. 2081–2084, Nov. 2013.

[14] H. Xu, L. Liu, and Y. Shi, "Polarization-insensitive four-channel coarse wavelength-division (de)multiplexer based on mach-zehnder interferometers with bent directional couplers and polarization rotators," *Opt. Lett.*, vol. 43, no. 7, pp. 1483–1486, Apr. 2018.

[15] Y. Xiong, D. X. Xu, J. H. Schmid, P. Cheben, S. Janz, and W. N. Ye, "Fabrication tolerant and broadband polarization splitter and rotator based on a taper-etched directional coupler," *Opt. Exp.*, vol. 22, no. 14, pp. 17458–17465, Jul. 2014.

[16] B. Bai, L. Liu, and Z. Zhou, "Ultracompact, high extinction ratio polarization beam splitter-rotator based on hybrid plasmonic-dielectric directional coupling," *Opt. Lett.*, vol. 42, no. 22, pp. 4752–4755, Nov. 2017.

[17] X. Guan, P. Chen, S. Chen, P. Xu, Y. Shi, and D. Dai, "Low-loss ultra-compact transverse-magnetic-pass polarizer with a silicon subwavelength grating waveguide," *Opt. Lett.*, vol. 39, no. 15, pp. 4514–4517, Aug. 2014.

[18] Y. Xiong, D.-X. Xu, J. H. Schmid, P. Cheben, and W. N. Ye, "High extinction ratio and broadband silicon TE-pass polarizer using subwavelength grating index engineering," *IEEE Photon. J.*, vol. 7, no. 5, Oct. 2015, Art. no. 7802107.

[19] J. Chi, H. Liu, N. Huang, and Z. Wang, "High-performance transverse magnetic mode-pass polarizer based on silicon nitride–silicon subwavelength grating waveguide for mid-infrared wavelengths," *Appl. Phys. Exp.*, vol. 11, no. 4, Mar. 2018, Art. no. 042005.

[20] B. Ni and J. Xiao, "Subwavelength-grating-based compact and broadband TE-pass polarizer for slot waveguides on a SOI platform," *J. Opt. Soc. Amer. B*, vol. 36, no. 8, pp. 2126–2133, Aug. 2019.

[21] M. Barona-Ruiz et al., "Broadband and low-loss TM-pass polarizer using tilted subwavelength structures," *Opt. Exp.*, vol. 30, no. 21, pp. 38930–38937, Oct. 2022.

[22] J.-M. Liu and D.-L. Zhang, "Ultra-broadband thin-film lithium niobate TM-pass waveguide polarizer using subwavelength grating metamaterial," *Opt. Laser Technol.*, vol. 164, Sep. 2023, Art. no. 109556.

[23] M. Barona-Ruiz et al., "High performance TM-pass polarizer via subwavelength grating bandgap engineering," in *Proc. IEEE Silicon Photon. Conf.*, 2023, pp. 1–2.

[24] G. Xiaowei, X. Peipeng, S. Yaocheng, and D. Daoxin, "Ultra-compact and ultra-broadband TE-pass polarizer with a silicon hybrid plasmonic waveguide," *Proc. SPIE*, vol. 8988, pp. 213–219, 2014.

[25] B. Bai, L. Liu, R. Chen, and Z. Zhou, "Low loss, compact TM-Pass polarizer based on hybrid plasmonic grating," *IEEE Photon. Technol. Lett.*, vol. 29, no. 7, pp. 607–610, Apr. 2017.

[26] B. Bai, F. Yang, and Z. Zhou, "Demonstration of an on-chip TE-pass polarizer using a silicon hybrid plasmonic grating," *Photon. Res.*, vol. 7, no. 3, pp. 289–293, Mar. 2019.

[27] B. Ni and J. Xiao, "Plasmonic-assisted TE-Pass polarizer for silicon-based slot waveguides," *IEEE Photon. Technol. Lett.*, vol. 30, no. 5, pp. 463–466, Mar. 2018.

[28] Y. Xu and J. Xiao, "A compact TE-Pass polarizer for silicon-based slot waveguides," *IEEE Photon. Technol. Lett.*, vol. 27, no. 19, pp. 2071–2074, Oct. 2015.

[29] J. R. Ong et al., "Broadband silicon polarization beam splitter with a high extinction ratio using a triple-bent-waveguide directional coupler," *Opt. Lett.*, vol. 42, no. 21, pp. 4450–4453, Nov. 2017.

[30] S. Wang et al., "Design of feasible Si-Si $_3$ N_4 interlayer polarization beam splitter toward 3D optical interconnect," *Proc. SPIE*, vol. 11617, pp. 502–507, 2020.

[31] H. Xu, D. Dai, and Y. Shi, "Anisotropic metamaterial-assisted all-silicon polarizer with 415-nm bandwidth," *Photon. Res.*, vol. 7, no. 12, pp. 1432–1439, Dec. 2019.

[32] H. Xu, D. Dai, and Y. Shi, "Ultra-broadband and ultra-compact on-chip silicon polarization beam splitter by using hetero-anisotropic metamaterials," *Laser Photon. Rev.*, vol. 13, no. 4, 2019, Art. no. 1800349.

[33] H. Zafar, P. Moreira, A. M. Taha, B. Paredes, M. S. Dahlem, and A. Khilo, "Compact silicon TE-pass polarizer using adiabatically-bent fully-etched waveguides," *Opt. Exp.*, vol. 26, no. 24, pp. 31850–31860, Nov. 2018.

[34] P. Chamorro-Posada, "Ultracompact integrated polarizers using bent asymmetric coupled waveguides," *Opt. Lett.*, vol. 44, no. 8, pp. 2040–2043, Apr. 2019.

[35] W. Liu, D. Dai, and Y. Shi, "All-silicon on-chip polarizer with$>$ 415 nm working bandwidth," in *Proc. IEEE 19th Int. Conf. Opt. Commun. Netw.*, 2021, pp. 1–2.

[36] H. Zafar et al., "Compact broadband (O, E, S, C, L & U bands) silicon TE-pass polarizer based on ridge waveguide adiabatic S-bends," *Opt. Exp.*, vol. 30, no. 6, pp. 10087–10095, Mar. 2022.

[37] J. F. Bauters, M. J. R. Heck, D. Dai, J. S. Barton, D. J. Blumenthal, and J. E. Bowers, "Ultralow-loss planar Si_3N_4 waveguide polarizers," *IEEE Photon. J.*, vol. 5, no. 1, Feb. 2013, Art. no. 6600207.

[38] W. Zhao et al., "Ultracompact silicon on-chip polarization controller," *Photon. Res.*, vol. 12, no. 2, pp. 183–193, Feb. 2024.

[39] W. Liu, S. Zhao, H. Li, D. Dai, and Y. Shi, "Ultra-high performance all-silicon TM polarizer covering O-U optical communication bands," *J. Lightw. Technol.*, vol. 40, no. 22, pp. 7326–7332, Nov. 2022.

[40] N. Dhingra and F. Dell'Olio, "Ultralow loss and high extinction ratio TM-Pass polarizer in silicon photonics," *IEEE Photon. J.*, vol. 12, no. 6, Dec. 2020, Art. no. 6602311.